A first-principles investigation on the enthalpy landscape for the hibonite solid solution: Implications for a nebular barometer

Pierre-Marie Zanetta, Abhishek Kumar Thakur, Venkateswara Rao Manga, Krishna Muralidharan, Thomas Zega

A first-principles investigation on the enthalpy landscape for the hibonite solid solution: Implications for a nebular barometer

Revision 1

Word count: 7966

Pierre-Marie Zanetta[1*], *Abhishek Kumar Thakur*[2], *Venkateswara Rao Manga*[1,2], *Krishna Muralidharan*[1,2], *Thomas J. Zega*[1,2]

1. Lunar and Planetary Laboratory, University of Arizona, 1629 E. University Blvd., Tucson, Arizona 85721, United States. 2. Materials Science and Engineering, University of Arizona, 1235 E. James E. Rogers Way, Tucson, Arizona 85721, United States.

*Send correspondence to pierre.marie.zanetta@gmail.com, *New address*: UMR5276 (CNRS, UCBL1, ENSLyon, UJM Saint-Etienne), 20 rue Dr Rémy Annino 42023 Saint-Etienne, France

Abstract

Hibonite, nominally $CaAl_{12}O_{19}$, is among the first minerals thermodynamically predicted to have formed in the early history of our solar system. It can incorporate significant amounts of Ti (≤15 wt%, ~2 cations per formula unit) into its crystal structure as both Ti^{4+} and Ti^{3+}. The main pathways for Ti incorporation in the solar nebula include a direct substitution of Ti^{3+} replacing Al^{3+} and a coupled substitution in which Ti^{4+} and Mg^{2+} replace two Al^{3+}. Additionally, the formation of oxygen vacancies can also reduce a Ti^{4+} cation to Ti^{3+} by trapping a free electron. The relative amounts of these cations potentially reflect the fugacity of oxygen (fO_2), a fundamental thermodynamic parameter, that prevailed when hibonite first formed or last equilibrated. However, the Ti content and its oxidation state in hibonite does not depend solely on fO_2. The composition of the system is, thus, a key factor in changing the $Ti^{4+}/\sum Ti$ ratio of the

structure concurrently with the fO_2. Therefore, it is necessary to understand the energetics, complex crystal chemistry, and substitution reactions of hibonite in order to relate the Ti oxidation state to the fO_2 of the nebular system in which condensed.

To that end, we report DFT calculations (0 K) to determine the ground-state energies and the enthalpy of formation (ΔH) of hibonite solid solutions that span the range reported in meteorites. Our results show that coupled substitution is energetically favored (ΔH=-96.70 kJ.mol^{-1}, from oxides). In comparison, the formation of oxygen vacancies is energetically unfavorable, but similar to Ti^{3+} direct substitution for Al^{3+} (ΔH=~60 kJ.mol^{-1}, from oxides), which is commonly observed in hibonite. It is therefore necessary to consider oxygen vacancies as a potential mechanism for controlling the incorporation of Ti^{3+} into hibonite, in addition to direct replacement reactions. We provide here the first reliable estimation of the formation enthalpies for the hibonite solid solution that includes solutes and point defects. The results presented herein constitute a significant advance towards the establishment of a comprehensive Gibbs free energy description of the hibonite solid solution, which is ultimately required for accurate modelling of its thermodynamic stability within the early solar nebula.

Keywords: Hibonite, density functional theory, enthalpy of formation, titanium, oxidation state, oxygen vacancies, early solar system.

1. Introduction

Hibonite is an oxide mineral with endmember stoichiometry $CaAl_{12}O_{19}$ that occurs in both terrestrial and extraterrestrial rocks. In terrestrial settings, hibonite occurs mostly in high metamorphic facies rocks ***(Curien et al. 1956; Bermanec et al. 1996; Nagashima et al. 2010; Holtstam and Hålenius 2020)***. In chondritic meteorites, hibonite occurs mainly in calcium-aluminum-rich inclusions (CAIs), but also in amoeboid olivine aggregates (AOAs), as presolar grains, or in the

matrix ***(Allen et al. 1978; Armstrong et al. 1982; Beckett et al. 1988; Brearley and Jones 1998; Zega et al. 2011)***. Hibonite is of particular importance in cosmochemistry because it is thermodynamically predicted to be among the first minerals to condense from a cooling gas of solar composition in the early solar protoplanetary disk ***(Kornacki and Fegley 1984; Geiger et al. 1988; Yoneda and Grossman 1995; Ebel 2006; Lodders and Palme 2009; Zega et al. 2021)***. Thus, its crystal chemistry can provide important information on the thermodynamic environments (P, T, fO_2) of the early solar system.

In CAIs, hibonite can incorporate Ti, Mg, Fe, V, and Si as solutes through varied pathways. Fe or Si (1 to 5 wt%) are mainly incorporated through secondary processes and so do not provide information on the primordial condensation parameters in the protoplanetary disk ***(Brearley and Jones 1998; Zanetta et al. 2023)***. Fe can be incorporated through thermal metamorphism and aqueous alteration whereas most Si-rich hibonite formed in Ti-free melts during repeated episodes of reheating in interactions with the surrounding nebular gas. In contrast, the substantial Ti and Mg substitutions (12-15 wt%, while V is in low concentration < 1 wt%) in minimally altered condensates are believed to occur via gas-solid reaction under the reducing conditions of the early solar system ***(Allen et al. 1978; Brearley and Jones 1998; Berry et al. 2017)***. Ti can occur in mixed oxidation states of Ti^{4+} and Ti^{3+}, and the relative amounts of these cations can be used to trace the fO_2 under which the hibonite formed or last equilibrated.

Ti^{3+} and Ti^{4+} can be incorporated into the structure mainly through two pathways ***(Allen et al. 1978; Brearley and Jones 1998)***. The primary pathway for Ti^{4+} is through a coupled substitution with Mg^{2+} and two Al^{3+} cations to maintain electroneutrality. In comparison, Ti^{3+} can substitute directly for Al^{3+}. In addition, oxygen vacancies can occur in the structure and play a key role in dictating the concentration of Ti^{3+} by trapping a free electron and reducing Ti^{4+} cations ***(Beckett et al. 1988; Asaduzzaman et al. 2021; Zanetta et al. 2023)***. Several papers report measurements of

Ti-oxidation states in hibonites from refractory inclusions in meteorites ***(Beckett et al. 1988; Simon et al. 2009; Zega et al. 2012; Giannini 2014; Han et al. 2022)*** and reveal that the $Ti^{4+}/\Sigma Ti$ ratio can vary significantly from 0.7 to 1. Such variations reflect the formation of hibonite grains in distinct environments in the solar protoplanetary disk. Thus, understanding and deciphering the Ti-substitution reactions in the pristine condensates is key to inferring precisely the thermodynamic conditions [P, T, fugacity of fO_2, chemical potentials] of the nebular gas when a hibonite grain originally condensed or last equilibrated.

However, there are potential challenges in using hibonite as an oxybarometer due to its complex crystal chemistry and the numerous solutes that can substitute into its structure ***(Doyle et al. 2014; Berry et al. 2017; Zanetta et al. 2023)***. The hibonite structure is part of the magnetoplumbite group (space group 194: $P6_3/mmc$) and is defined by 11 crystallographic sites, six of which are distinct Wyckoff sites. Of the 11 sites, six are occupied by cations; five are occupied by oxygen ***(Curien et al. 1956; Bermanec et al. 1996; Nagashima et al. 2010; Holtstam and Hålenius 2020)***. The $Ca_{(2d)}$ site is a 12-coordinated polyhedron. Al is distributed among five crystallographic sites labeled M1 to M5. The $M1_{(2a)}$, $M4_{(4f)}$, and $M5_{(12k)}$ are octahedra, $M3_{(4f)}$ is a tetrahedron, and M2 is a trigonal bipyramid with an ambiguity on its exact symmetry in the structure ***(Kreber et al. 1975; Obradors et al. 1985; Bermanec et al. 1996)***. The M2 site can adopt an ordered configuration in a 2b Wyckoff site or a 4e position with partial occupancy (a pseudo-tetrahedral site). The M1, M3, and M5 sites form a sequence of two cubic-closest-packed layers referred to as the spinel module (or S-block). The Ca, M2, and M4 sites form a sequence of three hexagonal closest-packed layers referred to a conductor layer or R-block ***(Nagashima et al. 2010)***.

To use hibonite as an oxybarometer, the role of substitution reactions and oxygen vacancy formation on its crystal chemistry and Ti oxidation state must be understood. To achieve such an objective, a comprehensive thermodynamic model of the crystal chemistry including major

solutes (Ti and Mg) and point defects (oxygen vacancies) on different sublattices (the possible M sites) is required. The establishment of such a thermodynamic model is impeded by two significant obstacles: 1) the complex crystal chemistry of hibonite precludes the synthesis of the entire solid solution while experimentally controlling the crystalline site of substitution; and as a result, 2) there are no thermochemical data available for the hibonite solid solution. To rectify those limitations, previous work investigated the Ti and Mg substitution and their location in the various M sites as well as the effect of the Ti oxidation state on the energetics of the hibonite solution through first-principles calculations employing the density-functional-theory (DFT) approach. ***(Doyle et al. 2014; Pankin et al. 2016; Asaduzzaman et al. 2021; Guerch et al. 2024)***. Pankin et al. (2016) investigated Ti substitution in their calculation, but limited their work to direct substitution, i.e., Ti^{3+} substituting for Al^{3+}. Doyle et al. (2014) investigated the energetics of the localization of the solute substitution and established that Ti should occur on the M2 or the M4 sites and Mg on the M3 site. Their results were later confirmed experimentally by Han et al. (2022) and Zanetta et al. (2023). However, in their calculation, Doyle et al. (2014) considered neither the case of mixed Ti^{3+} and Ti^{4+} in the same structure nor the occurrence of oxygen vacancies in controlling the Ti oxidation state. In a separate study, Asaduzzaman et al. (2021) included oxygen-vacancy formation in their calculations but considered a narrow range of hibonite compositions and substitution site combinations, providing a limited description of the enthalpy of formation of the hibonite solid solution. In addition to these complexities and the scarcity of thermochemical data, the results from previous DFT studies are not referenced against species in the same state and are therefore neither reproducible nor usable in a thermodynamic model.

To fill the knowledge gaps, here we investigate the complete interplay among the composition, the oxidation state of Ti, the substitution site, and oxygen-vacancy formation to

establish the thermochemistry of the hibonite solid solution. We also compare the energetics of direct substitution, coupled substitution, and oxygen vacancy formation, i.e., the three main substitution reactions, to quantify their potential to occur in the hibonite structure. This work is part of a broader effort to develop a comprehensive thermodynamic model of hibonite and infer the temperature and fO_2 under which it formed or last equilibrated in the solar protoplanetary disk. Such information can provide insight into the thermodynamic landscape of the inner and early solar system.

2. Methods

The thermodynamic properties and phase stability of a system can be calculated from the Gibbs free energy (ΔG), whether for endmember compositions or for discretized compositions in a range of solid solutions. Ideally, a free-energy description for hibonite would be obtained from experimental measurements. However, determination of the energetics of the entire range of hibonite solid-solution chemistry through experimental synthesis methods is impractical because of hibonite's complex crystal chemistry (several substitution sites). Moreover, experimentally regulating the Ti oxidation state in the structure is particularly complex since both the Mg activity and the oxygen fugacity affect it. Instead, density functional theory (DFT) offers an attractive alternative means of determining thermochemical and structural properties and provides accurate assessments of multiple properties from first principles ***(Kresse and Hafner 1993; Padilha et al. 2014; Liu et al. 2015; Pankin et al. 2016; Benisek and Dachs 2018, 2020; Asaduzzaman et al. 2021; Zega et al. 2021; Manga et al. 2022; Manga and Zega 2024)***.

Thermodynamic modeling of hibonite requires detailed knowledge of its thermochemistry, including the effects of the solutes in its structure. To obtain such information we defined structures to investigate the various compositions predicted to form from coupled substitution, single substitution, and formation of oxygen vacancies. Several considerations were necessary in

development of this model. The number of possible solutes and substitution sites being large in the hibonite structure, here we (1) focus on the most representative solutes (Ti and Mg) that occur in meteoritic hibonite in pristine CAIs, i.e., those that experienced little to no secondary alteration. Our model assumes that pristine hibonite does not incorporate substantial Si, Fe, and other elements into its structure during condensation in the solar protoplanetary disk but that these elements are instead introduced during substantial secondary thermal metamorphism or aqueous alteration, consistent with previous descriptions of pristine hibonite ***(Simon et al. 1997, 1999; Brearley and Jones 1998; Han et al. 2020; Zanetta et al. 2023)***. Further, we (2) limit the Ti and Mg substitutions to three Wyckoff sites (M2 and M4 for Ti and M3 for Mg), based on previous literature (e.g., Doyle et al., 2014, 2016; Han et al., 2022; Zanetta et al., 2023). We also assumed an initial (before relaxation) 2b position for the M2 site rather than a 4e position for our calculations ***(Bermanec et al. 1996; Nagashima et al. 2010; Holtstam and Hålenius 2020)***. We (3) considered the variation of the Ti^{3+}/Ti^{4+} ratio by the introduction of oxygen vacancies in the (M3) polyhedra on the $O4_{(12k)}$ site in the structure. We assumed that if an oxygen vacancy is formed, it would occur next to the Mg^{2+} cation substituting for an Al^{3+}. A single oxygen vacancy was created by removing an oxygen atom from the supercell, after which the supercell was energy-minimized. Based on these constraints, we defined 16 solid-solution compositions in which Ca, Al, Mg, and Ti solutes, vacancies, and substitution sites are represented. We investigated: (*i*) the direct replacement of Al^{3+} by Ti^{3+} on the M2 or the M4 sites; (*ii*) the coupled substitution of Ti and Mg alternating between the M2 and M4 sites for the Ti and keeping the Mg on M3 site; and (*iii*) the formation of oxygen vacancies on the O4 site associated with the Mg substitution on the M3 site while substituting Ti on the M2 or M4 sites respectively. We also investigated whether localization of two solutes substituting together in the structure could affect the total energy. Indeed, Mg and Ti, when they substitute together may occur in the M3 and M4 nearest sites, respectively, because those polyhedra, which are close together, could favor the

accommodation of the charges. To investigate such cases, we considered a "random" and "nearest" distribution of the Mg on M3 sites while incorporating Ti on the M4 site. Additional combinations were carried out to investigate the effect of the site occupancy and the concentration of the solute in the structure.

To provide a reference structure for the calculations, we initially optimized an endmember $CaAl_{12}O_{19}$ structure from Doyle et al. (2014) with 64 atoms (1×1×1) as a basis for the supercell structures (file from Item #AM-14-702 in the appendices of Doyle et al. (2014). The Brillouin Zone was then sampled using 2×2×1 supercell structure for a total of 256 atoms using Supercell software ***(Okhotnikov et al. 2016)***. Such large periodic lattices give rise to a vast number of combinations of similar structures where cations can substitute on equivalent positions. Therefore, to assess which of the combinations produced the smallest periodic unit (at atomic length scales), we characterized the structures through multisite correlation functions as described by Zunger et al. (1990) to produce special quasi-random structures (SQS). We employed supercell and Alloy Theoretic Automated Toolkit (ATAT) software to generate and rank the SQS structures (see Supp. Mat. section 1. for additional details).

The DFT approach to modeling thermochemical data has been described in detail ***(e.g., Turchi et al. 2007; Zega et al. 2021; Manga et al. 2022; Manga and Zega 2024)***. We used the projector-augmented plane wave pseudopotential method (PAW) as implemented in Vienna Ab initio Simulation Package (VASP) to relax our targeted SQS ***(Kresse and Furthmüller 1996)***. The PAW approach simplifies oscillating wavefunctions near the ion cores into smooth wavefunctions, allowing for greater computational efficiency. We used the Perdew–Burke–Ernzerh (PBE) post-DFT approach to treat the exchange and correlation energy and to determine optimized structures ***(Perdew and Zunger 1981; Perdew et al. 1996)***. The plane-wave cut-off energy was set to 400 eV, i.e, the cutoff on the number of plane-wave functions used to represent the

real electronic wavefunction. We used a force convergence, resulting from electromagnetic interactions between the atoms, of 0.05 eV/Å on each atom and an external pressure of less than 1 kBar. A k-point mesh of 4 × 4 × 2 is constructed using the Monkhorst-Pack scheme for Brillouin zone integration ***(Monkhorst and Pack 1976)***. All calculations are spin-polarized to account for the magnetic moment and a smearing width of 0.05 eV is used for electronic occupancy. After force and pressure convergence, a final calculation is performed using the tetrahedron method with Blöchl corrections to get an accurate total energy of each structure ***(Blöchl et al. 1994)***. We used SPGlib library to verify if the 194-space group symmetry (for further details on the adopted VASP symmetry preservation protocol, please refer to the supplementary material) was maintained ***(Togo and Tanaka 2018)***.

We used the "Bader" charge analysis to obtain the charge distribution of the SQSs after calculation and compare it with the expected charge from the crystal chemistry before ionic relaxation ***(Henkelman et al. 2006; Sanville et al. 2007; Tang et al. 2009; Yu and Trinkle 2011)***. The Jahn-Teller polyhedral distortion of each Wyckoff site was calculated based on:

$$\Delta d_x = \frac{1}{n}\sum_{i=1}^{n}\frac{(R-\bar{R})^2}{\bar{R}} \quad \#(1)$$

where Δd is the polyhedral distortion parameter; R is the individual cation (e.g., either Ca, Al, Ti or Mg) to oxygen (O) bond length (M-O) in the $(MO)_x$ polyhedron; and $\bar{R}$ is the mean M-O bond length in the $(MO)_x$ polyhedron ***(Manga et al. 2022)***. The n is the coordination number and can take the value 12, for Δd_{Ca} and its 12-coordinated polyhedron distortion parameter, n=6 for Ti on M4, n=5 for Ti on M2 and n=4 for Mg on M3.

The enthalpy of formation of the SQS is expressed as follow:

$$\Delta H_R{}^{0K} = E_0 - \sum_i^N C_i E_i^{mol} \quad \#(2)$$

Where E_0 is the ground-state energy of the considered SQS in J/mole, C_i is the concentration (molecular fraction) of the binary oxides i in the SQS structure and E_i^{mol} is the enthalpy of formation of the binary oxides in the same state. To compare with the literature, enthalpies of the solid solution series were referenced against their constituting oxides (i.e., CaO, Al_2O_3, TiO, Ti_2O_3 and MgO) as reference states ***(Zega et al. 2021)***. Those reference states exhibit minimal differences with thermochemical table (Δerr CaO=5.02, Δerr Al_2O_3=-1.90, Δerr Ti_2O_3=10.73, Δerr TiO_2=11.44, Δerr MgO=-2.71 in g-atom, e.g., Barin (1995)).

We assumed the general reaction;

$$CaO + ½\ w\ Al_2O_3 + x_1\ TiO_2 + ½\ x_2\ Ti_2O_3 + y\ MgO \rightleftharpoons CaAl_wTi_xMg_yO_z \quad (3)$$

with, w=12-(x+y), x=x_1 + x_2, and z = 1 + (3×½w) + (2×x_1) + (3×½x_2) + y).

$$\text{Thus, } \Delta H_{mix} = \Delta H_R - (\Delta H_{f\ CaO} + w_{/2}\ \Delta H_{f\ Al2O3} + x_1\ \Delta H_{f\ TiO2} + x_2\ \Delta H_{f\ TiO} + y\ \Delta H_{f\ MgO}) \quad (4)$$

Oxygen vacancies were included in those calculations by mixing the binary oxides to obtain charge neutrality (thus, z may differ from 19).

3. Results

Structure optimisation and ground state energies

We first relaxed the endmember $CaAl_{12}O_{19}$ (n°0) hibonite structure (Fig. 1, Table 1) using complete geometrical degrees of freedom (ionic positions, cell shape, and cell volume) while retaining the symmetry. Final positions can be found in Table 1 and are compared to the literature ***(Nagashima et al. 2010; Doyle et al. 2014)***. The maximum difference between our

calculations and Doyle et al. (2014) occur for O3 (±2.3e-4 Å for x and y direction), followed by O4 and Al4 (~1e-4 Å). The differences are greater than Nagashima et al. (2010), with 7.2e-3 Å for Al2, and (~±2.5e-4 Å) for O4, O3, and Al4 (Fig. 1). We note that in the experimental work from Nagashima et al. (2010), temperature has an effect on the atomic positions that are not integrated into the 0 K calculations presented in this work.

In contrast, the relaxation of SQS structures were obtained by following a symmetry-preserved scheme wherein the volume of the cell and ionic positions are allowed to relax, in alternative steps, to achieve the desired total pressure (< 1 kB) and forces (< 0.005 eV/Å). It is known that relaxation of SQS, with all geometrical degrees of freedom in a single run, can lead to changes in the symmetry of the cell. Therefore, relaxation with alternating volume and ionic-position enables monitoring of the evolution of energies while preserving the symmetry. Table 2 shows the 16 defined compositions of hibonite solid solutions and their final lattice parameters after the relaxation. Atomic positions and deviations from the original position (space group 194) were inspected. All SQS preserved the 194 spacegroup with a tolerance of 0.2 Å for each atomic equivalent position. The introduction of Ti, Mg, and O vacancies in the structure modify the cell parameters a/b and c (Table 2 and Fig. S1a) by +1% for calculations with no point defects (upper part of the Table 2). In comparison, the change in the lattice parameter (a/b and c) is +0.1% on average when only O vacancies are introduced in the structure. Most SQS structures containing oxygen vacancies show similar or smaller a/b and c parameters compared to endmember (n°0). The general tendency is that the higher the concentration of cations introduced into the structure, the higher the volume (e.g., Table 2 and Fig. S1a). The ground state energy (E_0) varies according to the number and type of substitutions. The more solutes that substitute into the structure, the more the ground state energy decreases (Table 2, Fig. S1b).

253 The introduction of solutes in the structure modifies the atomic positions and distorts the
254 crystal polyhedra (Fig.2 and Table S1, S2). The M2 polyhedra exhibit the largest distortions (Δd)
255 independently of where the solutes are substituted in the structure (Fig 2, the sum of the brown
256 and orange bins is significantly larger than the bin of any other polyhedron). Although we setup
257 the M2 position to be on a 2b Wyckoff site, relaxation caused it to occupy a different position
258 than its initial central position (Fig. 1 and Table 1). The new 4e position (with a partial
259 occupancy, see Fig. S2) strongly distorts the polyhedron (Fig. 2, and Table S1, S2) and modifies
260 the bond distances between the M2 central cation and the O1 atoms (above and below the central
261 position, Table S1, Fig. S2). The polyhedron M2 is deformed at its maximum when Ti occurs on
262 the M4 site only (Fig. 2 and Table S2). The polyhedra are less distorted and the central atom is
263 closer to a 2b position when Ti occurs on the M2 site (Fig. 2). Structures containing oxygen
264 vacancies show the lowest distortion. Oxygen vacancies have the effect of increasing the
265 maximum bonding distance between the central cation and the oxygen at the M3 site. However,
266 this distortion remains minimal in comparison to other crystal sites. Deformation is only slightly
267 accommodated at the M3 site.

268 During the relaxation, most of the deformation due to cation substitutions in the structure
269 was accommodated in the R-block (Ca, M2, and M4 sites, e.g., Fig. 3a). In comparison, the M1,
270 M3, and M5 sites, i.e., the S-block, display smaller distortion, even for a high concentration of
271 solutes and when oxygen vacancies occur in the M3 polyhedra (Fig. 2 and Table S2). The M5
272 site that is at the interface between the S-block and the R-block shows higher distortion than the
273 M1 and M3 polyhedra (Fig.2 and Table S2). There is a dichotomy in how the total energy is
274 affected by distortion if it occurs in either the S-block or the R-block (Fig. 3b). The energy of the
275 structure can be minimal even for significant distortion ($\Delta d > 0.1$) occurring in the R-block (Fig.

3b). On the contrary, smaller variations ($\Delta d>0.005$) in the S-block significantly destabilize the structure and increases its total energy ($\Delta E=150$ eV).

Bader analysis

The Bader charge, derived from the electron density from VASP calculations, is useful to determine the impact of the substitutions on the charge distribution ***(Henkelman et al. 2006; Sanville et al. 2007; Tang et al. 2009; Yu and Trinkle 2011)***. Bader-charge analysis is a necessary step to compare with the theoretical formula before ionic relaxation and the crystal chemistry obtained by calculation. We selected six SQS of interest to quantify the Ti oxidation state after relaxation and check that it is consistent with stoichiometry and charge neutrality. We used the $CaAl_{12}O_{19}$ endmember as a reference to establish Al, O, and Ca charge equivalence (Table 3). The Al and O charges are close to nominal, i.e., 3^+ and approximately 2^-, respectively. In comparison, the Ca shows a Bader charge of approximately 1.6+.

In the case of Ti in hibonite structure, SQS n°8 serves as a reference because that structure has Ti substituting on M4 and no other cations are substituting on other sites. In SQS n°8, the Ti charge is expected to be 3^+ based on stoichiometry and assuming charge neutrality. Bader-charge analysis shows a charge of 2.3^+ for all Ti sites. Thus, we first established that a Bader charge of 2.3^+ corresponds to 3^+ for Ti cation in the structure, e.g., SQS n° 6 and 8. Mg shows a nominal Mg^{2+} Bader charge. Structures that contain Mg should therefore contain associated Ti^{4+} (according to the charge neutrality rule) and display a higher Bader charges, e.g., 2.7 for SQS n°9, 10, and 16 in contrast to the 2.3^+ for Ti^{3+}. Charge difference due to Ti substitution can be found in supplementary material (Fig. S3, S4). The introduction of oxygen vacancies affects the Ti Bader charge (Table 3, SQS n°16). Ti next to the vacancies show a lower Bader charge of 2.5 while other Ti away from the vacancies show Bader charge of 2.7. The

introduction of vacancies does not affect the average O4 Bader charge (-2.06) but they significantly affect the local O4 Bader charge with individual O4 exhibiting the lowest charge of -2.6 while a minimum of -2.0 is observed for all the other structures (Table 3, SQS n°16). Currently, it is difficult to ascertain the oxidation state of a cation situated within a precise Wyckoff site and to determine the influence exerted by the nearest oxygen vacancy on site distortion through empirical means. Thus, it is difficult to compare our Bader-charge analysis to experimental data. The only existing data that quantified the Ti oxidation at the atomic scale in meteoritic hibonite were previously collected by ***(Zanetta et al. 2023)***. In their paper, ***Zanetta et al. (2023)*** were able to highlight the potential presence of oxygen vacancies using charge neutrality. However, we note that the errors in quantifying these parameters at this scale are quite significant.

Enthalpy of formation

We provide a first estimation of the enthalpy of formation for the hibonite solid solution. The enthalpy of formation was determined for each structure from the ground state energy obtained by first-principle calculations (Fig. 4 and Table 2). A 3D representation of the Al – Mg – Ti ternary diagram is shown in Figure 4. SQS structures show higher and lower $\Delta H_{mixNorm}$ than the endmember (n°0) used as the reference state with values ranging from 60 to 212 kJ/mole (see also Table 2). The structures that display the lowest energy are those that have Ti as Ti^{4+}, i.e., a $Ti^{4+}/\sum Ti$ close to 1, and Mg in relatively high concentration in their structure (e.g., SQS n°1, 9, and 10, see Table 2). The coupled substitution (for instance SQS n°1 to 5, 9 and 10) of Mg^{2+}+ Ti^{4+} is energetically favored in comparison to direct substitution of Ti^{3+} (SQS n°6) or the reduction of Ti^{4+} to Ti^{3+} via oxygen vacancy formation (SQS n°12-16, Table 2).

SQS n°1 to 5 have similar compositions with a total Ti concentration of 1 cation per formula unit (p.f.u), with Ti^{4+} occupying the M2 site, the M4 site, or distributed between both sites. The enthalpy of formation is relatively similar for those five structures (Table 2). We also find similar $\Delta H_{mixNorm}$ for structures containing Ti^{3+} substituted on the M2 or the M4 sites (SQS n°14 vs 15). In other words, our calculations suggest that the enthalpy of formation is weakly dependent on the Ti substitution site for Ti = 1 cation p.f.u, even if a slightly lower energy is observed on the M2 site (SQS n°1). On the contrary, when Ti is highly concentrated (Ti = 2 cation p.f.u, SQS n°10) it can fully occupy the M4 site and a significantly lower energy is observed.

The compositions containing the same concentration of Ti on a single site, with or without Mg, show similar formation energies (Table 2, SQS n°2 vs n°8). Thus, the Mg concentration does not change the enthalpy of formation. Also, the "nearest" and "random" Mg substitution (along with Ti on M4) structures show that there is no difference in energy among structures with the same composition in which Mg occurs next to the substituted Ti or is randomly distributed on the M3 Wyckoff site (Table 2). Thus, the computations suggest that mixing of Mg and Ti on M3 and M4, respectively, do not exhibit any association and can prefer random arrangement on their respective Wyckoff sites.

It is likely that the occurrence of oxygen vacancies increases the total energy due to the perturbation of the atomic symmetry in the structure. Table 2 shows that the oxygen vacancy calculations (for the structure that we defined) exhibit higher total energy than the endmember n°0 and solid solutions. For instance, SQS n°10 and n°16 show similar composition (full occupancy of the M4 and M3 sites by Ti and Mg respectively), but SQS n°16 contains oxygen vacancies in the M3 polyhedra and shows a significantly higher enthalpy ($\Delta H_{mixNorm}$=66.78 kJ/mol vs -96.70 kJ/mol). However, we note that SQS n°8, which models a single substitution

(Ti^{3+} for Al^{3+}) reaction, shows a $\Delta H_{mixNorm}$= 60.68 kJ/mol which is close to the $\Delta H_{mixNorm}$= 66.78 kJ/mol of the SQS n°16 that models the reduction of Ti^{4+} to Ti^{3+} due to the introduction of an oxygen vacancy.

4. Discussion

Site occupancy analysis

We computed enthalpies of mixing for a range of hibonite solid solutions in our effort to develop its thermodynamic model for nebular conditions. We constrained the number of substitution sites of the solutes (Ti and Mg) based on previous work ***(Doyle et al. 2014)***, enabling investigation of a more comprehensive set of structures for these sites. We discuss the new observations that have been enabled by the extended data set to previous models. First, our calculations show that Ti substitution in the hibonite structure is energetically favored for the simulated structures, consistent with previous descriptions ***(Doyle et al. 2014; Pankin et al. 2016; Asaduzzaman et al. 2021)***. This result is also consistent with the relatively high concentration of Ti (up to 12 wt%) measured in natural samples ***(Allen et al. 1978; Armstrong et al. 1982; Beckett et al. 1988; Bermanec et al. 1996; Brearley and Jones 1998)***. Second, our calculations provide insight on the effect of Ti concentration on site preference. We observed that for a low level (<1pfu) of substitution, Ti^{4+} would preferentially occupy the M2 site, whereas in samples with high Ti content (2 cation p.f.u), Ti^{4+} prefers neighboring M4 sites. Similar results were obtained in previous calculations from Doyle et al. (2014) as well as microprobe and Rietveld refinements by Berry et al. (2017). Doyle et al. (2014) suggested that this concentration dependence is mostly due to Ti-Ti interactions, i.e., that Ti^{4+} on two neighboring M4 sites would lower the ground state energies. In comparison, we suggest that the concentration dependency of the Ti site preference is instead due to the multiplicity of the site. For low Ti^{4+} concentration, the M2 site would be

favorable (in comparison to M4) because of the lower multiplicity of the site, which would tend to populate faster and attain a full occupancy during crystallization. For a higher concentration of Ti^{4+}, and if Mg is available, Ti^{4+} can fully occupy the M4 site and stabilize the structure (e.g., SQS n°10, Table 2). We note that in the cases of low Ti concentration (Ti=1 cation p.f.u), the difference in energy of the structures where the Ti is distributed on the M2 site (SQS 1) or on both M2 and M4 sites (SQS 4 and 5), is small (0.1 eV/f.u.). If the Ti is distributed over the M2 and M4 site (SQS 4 and 5), and thus adopts a partial occupancy of the M2 site, it implies a possible gain in configurational entropy. This small change in configurational entropy could be sufficient to change the site preference. Such reasoning does not apply to the case in which Ti concentration is high and fully occupying the M4 site (Ti=2 cation p.f.u) because the energy difference is significant (few eV/f.u., e.g., SQS n°10 and 11). Third, our work shows that Mg and Ti do not require substitution on nearby sites, suggesting that the Ti-Mg interactions are weak and which might be explained by the relatively long distance (3.55 Å) between the two sites. Fourth, we find that the case of mixed Ti oxidation state within the same SQS (which was not investigated in previous DFT work) is the most favorable ground state energy (SQS, n°11). Ultimately, our extended SQS series shows a lower Ti bader charge (Ti^{3+}) if a vacancy is located on the nearby M3 polyhedra and demonstrates that we correctly modelled the reduction of Ti^{4+} to Ti^{3+} by trapping a free electron. These results were not modelled previously, even in the earlier work of Asaduzzaman et al. (2021), since only the vacancies adjacent to the Ti atoms affected the system in their modelling. We could not investigate how Ti^{3+} and Ti^{4+} distribute between the two sites (M2 and M4) in the case of a mixed oxidation state (i.e., without oxygen vacancies) because our Bader analysis was not conclusive (intermediate charge for all Ti atoms see supplementary material) potentially due to the limited size of our supercell. However, it is possible that Ti^{3+} and Ti^{4+} would be distributed on both sites as significant $Ti^{4+}/\sum Ti$ variation over the M2 and M4 sites was measured in an atomic-scale study by Zanetta et al. (2023).

393 The compositional range that we investigate here sheds new lights on two important
394 characteristics of the hibonite structure. First, the effect of the polyhedral distortion on the total
395 energy is dependent on the specific block within the hibonite structure where the distortion
396 occurs. Almost no distortion is accommodated in the S-block and the energy of the structure is
397 minimal even if significant distortion occurs in the R-block (Fig. 3b). Previous work from
398 Nagashima et al. (2010) reported a dichotomy in the behavior of the hibonite structural blocks.
399 They experimentally compared the evolution of the S-block and the R-block volume in the
400 hibonite structure as a function of temperature. They showed that the expansion of the R-block
401 with the temperature is steeper than that of the S-block. Our results appear to explain this
402 dichotomy, i.e., the different responses of the R- and S-block are due to impurity substitution and
403 resulting polyhedral distortions. Both blocks efficiently fill the space (up to 74%) since the S-
404 block is a sequence of two cubic closest-packed layers (cc) and the R-block is a sequence of
405 three hexagonal closest-packed layers (Fig. 1). The solutes (Ti and Mg), should change the
406 volumes in a similar way in both blocks. We hypothesize that the S-block has a greater bond-
407 stiffness due to an overall lower coordination (tetrahedron and octahedra vs trigonal, octahedra,
408 and 12-coordinated polyhedron) of the sites that compose it. Such bond stiffness could thus
409 explain why most of the distortion is preferentially accommodated in the R-block. In
410 comparison, bond softness in the R-block is evidenced, for example, by a strong dynamic
411 disorder of the Ca site at high temperature, with a stronger motion for Ca than for the
412 coordinating light oxygen atoms ***(Nagashima et al. 2010)***. Second, the introduction of solutes in
413 the structure force the M2 central atom to move to a 4e position. This M2 asymmetric position
414 closely matches the atomic position measured by Nagashima et al. (2010). Such displacement is
415 usually attributed to atomic vibration and is a frequent problem in XRD analyses of the
416 magnetoplumbite-type structures (e.g., Kreber et al., 1975; Obradors et al., 1985; Bermanec et
417 al., 1996). Our results show that the volume around the M2 polyhedron gives this

crystallographic site a large diversity of local minima energy potential. We note that the displacement of the central 2b position to a 4e position (with partial occupancy of 1/2) was forced by the substitution of the solute and energetically favored at 0 K (Table 2, Fig. 2, Fig. S2). The vibrational activity is thus not a requirement to explain this alternative position. The displacement of the M2 central atom due to impurities at 0K show that the composition might partly control this ambiguity. We also note that if 2b and 4e have nearly identical enthalpies, then 4e may become favorable at finite temperatures because it gains configurational entropy as the site become partially filled (to maintain the number of atoms per unit cell).

Standard enthalpy of formation

The scarcity of experimental data on the thermochemistry of hibonite and the fact that these studies have only focused on nominal hibonite ($CaAl_{12}O_{19}$), underscores the significance of this research. To our knowledge, these findings represent the first reliable estimates of the energetics associated with the hibonite solid solution (Ti and Mg pole), referenced from species in the same state, paving the way for the modeling of complex compositions. It is challenging to corroborate these findings with an alternative methodology because there is a dearth of experimental data pertaining to the energetics of a hibonite structure incorporating Ti and Mg at defined substitution sites. However, our calculations are consistent with existing literature values for the nominal composition for which experimental data are available. The enthalpy of formation of our endmember $CaAl_{12}O_{19}$ ΔH_{mix} = -10,644.2 ± 67 kJ.mol^{-1} (0 K, from elements) is in the range of previous experimental values and those derived from phase-diagram analysis, i.e., $\Delta H_f \sim$ [-10,600, -10,800] kJ.mol^{-1} (298 K; from elements, Table 4, e.g., ***(Glushko 1979; Eliezer et al. 1981; Eliezer 1982; Hemingway 1982; Geiger et al. 1988; Hallstedl 1990; Eriksson and Pelton 1993)***).

The enthalpy energies derived in this work cannot be directly used to calculate the Gibbs free energy and compared with thermochemical data in the literature for nominal hibonite. To do so, the entropic contribution must first be determined ($\Delta G = \Delta H - \mathbf{T\Delta S}$). The lattice models used in this work have the advantage of determining the enthalpy of a complete series of solid solutions with constrained substitution sites. These unusual hibonite solid solutions are too complex for a comprehensive synthesis and detailed calorimetry measurement. Therefore, DFT computes entropic contributions using the Debye-Gruneisen or phonon calculation approach to account for structural perturbations because they directly affect the thermochemical properties of the materials ***(Moruzzi et al. 1988; Lu et al. 2005, 2007)***. Based on these new enthalpies of formation and by calculating the effects of the entropic component of the system, it will be possible, in future work, to estimate the Gibbs free energies of the system containing Mg, Ti, and O vacancies and to compare these energies with existing thermochemical data for nominal hibonite ***(Blander and Fuchs 1975; Allibert et al. 1981; Kornacki and Fegley 1984; Kumar and Kay 1985; Nagata et al. 1989; Hallstedl 1990; Eriksson and Pelton 1993)***. Ultimately, these results will be integrated into a thermodynamic model containing thermochemical data for other stable refractory phases around the condensation temperatures and pressures of hibonite.

Many recent articles have suggested that DFT with the generalized-gradient approximation does not provide the correct ground state energy for the oxides. The current opinion is that a Hubbard U correction improves the DFT results. Wang et al. (2006) defined the U parameter by computing the energy of a large number of oxidation reactions of 3d transition metal oxides using the generalized gradient approach (GGA) and GGA+U methods. Two substantial contributions to the error in GGA oxidation energies were identified and they proposed a systematic correction for the O_2 molecule energies of -1.36 eV that we applied to our data when normalizing from the elements ***(Zhang et al. 2018)***. Such correction gives a match with

a ΔH_{f0} in range with previous literature (Table 4). It is difficult to quantify precisely the errors inherent in DFT calculations (see Supp. Mat 2 and Manga and Zega, 2024, for a precise estimate of errors from k-mesh of different sizes and various plane-wave-energy cutoffs) and most of the time a relative calibration is given from experimental studies. Here, comparison with previous literature gives a difference of less than 5-10 kJ/g-atom. ***(Barin 1995; Manga and Zega 2024)***. The correct referencing of first principle calculations is fundamental in order to be usable as a database for future work but also to be reproducible and available for the community. Such appropriately referenced calculation allows a reliable benchmarking with experimental data and are at the basis of the Calculation of Phase Diagrams (CALPHAD) approach. Previous studies, lacking reference states, could not be quantitatively compared to our thermochemical data despite providing critical clues on the crystal chemistry of hibonite ***(Doyle et al. 2014; Pankin et al. 2016; Asaduzzaman et al. 2021)***.

With the above caveats in mind, the determination of enthalpy of formation sheds light on the thermodynamic stability of Ti-bearing hibonite. If all of the structures are compared, the coupled substitution of Ti^{4+} with Mg^{2+}, independent of their position in the structure, is the most energetically favorable pathway for Ti incorporation (Table 2 and Fig. 4). If no specific thermodynamic conditions are imposed on the hibonite-forming system, then the most stable phase to form would be enriched in Ti^{4+} + Mg^{2+} with Ti occupying the M4 site. If Mg and Ti are sufficiently available in the system, a full occupancy of the M3 and M4 sites would be favored to preserve the symmetry (noted in SQS N°10, -96.70 kJ.mol-1). In comparison, for similar hibonite compositions, we find that the enthalpy of formation is significantly affected by the presence of oxygen vacancies, e.g., SQS n°16 (containing oxygen vacancies) = 66.77 kJ/mol versus SQS n°10 (no oxygen vacancies) = -96.70 $kJ.mol^{-1}$ (Table 2). Now, if the energy of this structure (n°16) containing oxygen vacancies is compared to the energy of formation of a

structure mimicking the direct substitution of Ti^{3+} for Al^{3+} (SQS n°16 to SQS n°8), then we obtain similar enthalpy of formation (~60kJ/mol). The similar energetics for the reactions involving direct substitution and the oxygen vacancy formation (reducing Ti^{4+} to Ti^{3+}) demonstrates that both reactions are nearly equally energetically unfavorable but whether they proceed to completion depends critically on the thermodynamic conditions of the system.

Cosmochemical Implications

Hibonite was proposed as an oxybarometer that can provide an indication of the fO_2 conditions prevalent at the time the first solids formed 4.5673 Ga ago ***(Beckett et al. 1988; Amelin et al. 2002, 2009; Connelly et al. 2012; Berry et al. 2017; Zanetta et al. 2023)***. Previously, we concluded that use of hibonite as a universal oxybarometer requires a complete thermodynamic description of the solid solution in its entire composition space, including the role of oxygen vacancies ***(Zanetta et al. 2023)***. Here we show the importance of such a model. Interpretations based on enthalpy predictions from this work indicate that the coupled Ti^{4+} + Mg^{2+} substitution is the favorable reaction to incorporate Ti into the hibonite structure. However, free energies with the included entropic contributions into various defect reactions will enable an accurate prediction of the stable crystal chemistry. In meteoritic hibonite, a well-known Ti:Mg 1:1 correlation is systematically observed ***(Allen et al. 1978; Armstrong et al. 1982; Doyle et al. 2014; Berry et al. 2017; Han et al. 2022; Zanetta et al. 2023)***, suggesting that coupled substitution is the most likely pathway for the incorporation of Ti^{4+} into the hibonite structure. Yet, in natural samples, Ti^{3+} was also measured in relatively high concentration (~1 Ti_2O_3 wt% ***(Beckett et al. 1988; Han et al. 2022; Zanetta et al. 2023)***). Therefore, at least one alternative reaction introduced Ti^{3+} into the structure of hibonite under nebular conditions. Berry et al. (2017) suggested that because of the prevalence of the coupled substitution, the Ti oxidation state was mostly controlled by the Mg activity. Although the Mg activity plays a key role, the oxygen fugacity,

may, in certain cases, become the main factor driving the previously described reactions. The early solar system was marked by significantly reducing conditions with log fO_2 = -18.1 (at T=1500K), which is six orders of magnitude lower than the iron-wüstite buffer ***(Grossman et al. 2008)***. Such conditions could overcome the energy barrier and lead to one of the reactions introducing Ti^{3+} into the hibonite structure, e.g., the direct substitution or the formation of oxygen vacancies.

To explain the presence of the Ti^{3+} in the structure, previous literature invoked direct substitution under reducing conditions ***(Allen et al. 1978; Bermanec et al. 1996; Brearley and Jones 1998)***. Here we show quantitatively for the first time that the reaction forming oxygen vacancies can occur in hibonite during its crystallization in the solar nebula with a similar enthalpy of formation ($\Delta H = \sim 60$ kJ.mol^{-1}, from oxides) as the direct Ti-substitution reaction. The oxygen vacancy formation is of great significance in the understanding of the early solar system thermodynamic landscape as it is directly linked to the oxygen fugacity of the solar gas in which the mineral formed during the process of primordial condensation. A noteworthy property of the two proposed reactions incorporating Ti^{3+} is that they are site specific. The oxygen vacancy mechanism could reduce some of the Ti^{4+} (by trapping a free electron), already present in the structure after having substituted along with Mg, and thus occupying the M4 site (if Ti is highly concentrated). Such a mechanism could therefore enrich the Ti^{3+} in the M4 site. On the contrary, direct Ti^{3+} substitutions are likely to happen on the M2 site because the M4 site would be preferentially filled (with Ti^{4+}) by coupled substitution. This second mechanism could therefore enrich Ti^{3+} on the M2 site. The predominance of these reactions in the protoplanetary disk may be recorded on the M2 or M4 site in natural hibonite, depending on the abundance of the Ti^{3+}. The precise quantification of the Ti^{4+} and Ti^{3+} distribution in natural samples could therefore give important constraints on which reaction dominated and on the fO_2 recorded in CAIs ***(Zanetta***

536 ***et al. 2023)***. We note that the record of these reducing conditions would only be retrievable in
537 pristine hibonites that have not been re-equilibrated in more oxidizing conditions.

538 Further, to evaluate the likelihood of either of these reactions to occur, a complete
539 thermodynamic model incorporating the entropic contributions to the free-energy function is
540 needed. The computation of enthalpy that we report on here is an important step in this direction
541 and should provide new insights into open questions. For example, how would Ti and Mg
542 substitution affect the condensation behavior of hibonite? Does the initially formed hibonite
543 contain Ti and/or Mg? How do the concentrations of these elements evolve as hibonite
544 condensation proceeds? Does the incorporation of Ti into hibonite affect the condensation of
545 perovskite? The newly derived thermodynamic data should ultimately provide answers to these
546 questions. Once the free-energy function incorporating the full range of solid solutions and
547 structural perturbations is determined, a thermodynamic model can be established. Such a model
548 will be a fundamental to providing new insights into the thermodynamic conditions that
549 prevailed in the early Solar System and the nature of the gaseous reservoir that formed the
550 planets.

551 **5. Conclusions**

552 Using density-functional theory (DFT), we determined the ground-state energy and the
553 enthalpies of formation of hibonite solid solution phases that span the range of compositions
554 reported for meteoritic hibonites. Our calculations provide a fundamental understanding on the
555 interplay among changes in composition, site substitution, and the oxidation state of titanium in
556 hibonite while incorporating the occurrence of oxygen vacancies in the system. The data show
557 that the formation of oxygen vacancies should be considered as a possible reaction to incorporate
558 Ti^{3+} in the structure along with the direct substitution of Ti^{3+} for Al^{3+}, especially under the

thermodynamic conditions that prevailed in the early solar nebula. The oxygen vacancy mechanism should result in an increase in the Ti^{3+} content on the M4 site, whereas direct Ti^{3+} substitutions are likely to occur on the M2 site. The advent of sophisticated microscopy tools, such as aberration-corrected scanning transmission electron microscopes, allows for direct probing of atomic structure and validation of the site occupancies suggested in this work. DFT calculations in conjunction with such atomic characterization will facilitate a better understanding of the first solid condensates. The estimate of enthalpies for the solid solution of hibonite (i.e., including solutes) provides a first stepping stone towards a full description of the free energy of this important phase and its development as a barometer.

6. Acknowlegements

Research supported by the NASA Emerging Worlds Program (80NSSC19K0509). Resources supporting this work were provided by the NASA High-End Computing (HEC) Program through the NASA Advanced Supercomputing (NAS) Division at Ames Research Center. We also acknowledge the High-Performance Computing (HPC) resources at the University of Arizona supported by the University Information and Technology Service We gratefully acknowledge NASA (grants #NNX12AL47G and #NNX15AJ22G) and NSF (grant #1531243) for funding of the instrumentation in the Kuiper-Arizona Laboratory for Astromaterials Analysis at the Lunar and Planetary Laboratory, University of Arizona. We thank members of the Planetary Materials Research Group at LPL for helpful discussions. We thank Matthieu Roskosz for his valuable input and guidance on the submission of this manuscript. Comments of the reviewers Andrew M. Davis and three anonymous reviewers, and of the associate editor Jianwai Wang significantly improved the manuscript and are highly appreciated.

7. Supplementary material.

The supplementary material contains 1) additional information about the use of correlation functions to maximize solute randomness in the SQS, 2) additional information about Vasp calculations and the reference states used in this manuscript. 3) Additional figures that may ease the understanding of the data presented in this manuscript. Additional Data are available at: https://data.mendeley.com/preview/v66nz2ynbs?a=4313a7ab-ccf6-4e7c-825d-61178c2dc498

Scripts are available at: https://github.com/ZanettaPM/DFT-Crystal-structure-evaluation

Ranking SQS bash code is available at: https://github.com/ZanettaPM/SQS-ranking-code

8. References

Allen, J.M., Grossman, L., Davis, A.M., and Hutcheon, I.D. (1978) Mineralogy, textures and mode of formation of a hibonite-bearing Allende inclusion. Lunar and Planetary Science Conference Proceedings, 9, 1209–1233.

Allibert, M., Chatillon, C., Jacob, K.T., and Lourtau, R. (1981) Mass-Spectrometric and Electrochemical Studies of Thermodynamic Properties of Liquid and Solid Phases in the System CaO-Al2O3. Journal of the American Ceramic Society, 64, 307–314.

Amelin, Y., Krot, A.N., Hutcheon, I.D., and Ulyanov, A.A. (2002) Lead Isotopic Ages of Chondrules and Calcium-Aluminum-Rich Inclusions. Science, 297, 1678–1683.

Amelin, Y., Connelly, J., Zartman, R.E., Chen, J.H., Göpel, C., and Neymark, L.A. (2009) Modern U-Pb chronometry of meteorites: Advancing to higher time resolution reveals new problems. Geochimica et Cosmochimica Acta, 73, 5212–5223.

Armstrong, J.T., Meeker, G.P., Huneke, J.C., and Wasserburg, G.J. (1982) The Blue Angel: I. The mineralogy and petrogenesis of a hibonite inclusion from the Murchison meteorite. Geochimica et Cosmochimica Acta, 46, 575–595.

Asaduzzaman, A., Muralidharan, K., and Zega, T.J. (2021) Density Functional Theory Driven Analysis of the Interplay among Structure, Composition, and Oxidation State of Titanium in Hibonite, Spinel, and Perovskite. ACS Earth and Space Chemistry, 5, 544–552.

Barin, I. (1995) Thermochemical Data of Pure Substances. Wiley.

Beckett, J.R., Live, D., Tsay, F.D., Grossman, L., and Stolper, E. (1988) Ti3+ in meteoritic and synthetic hibonite. Geochimica et Cosmochimica Acta, 52, 1479–1495.

Benisek, A., and Dachs, E. (2018) The accuracy of standard enthalpies and entropies for phases of petrological interest derived from density-functional calculations. Contributions to Mineralogy and Petrology, 173, 1–11.

Benisek, A., and Dachs, E. (2020) Excess enthalpy of mixing of mineral solid solutions derived from density-functional calculations, 47, 15.

Bermanec, V., Holtstam, D., Sturman, D., Criddle, A.J., Back, M.E., and Šćavničar, S. (1996) Nežilovite, a new member of the magnetoplumbite group, and the crystal chemistry of magnetoplumbite and hibonite. Canadian Mineralogist, 34, 1287–1297.

Berry, A.J., Schofield, P.F., Kravtsova, A.N., Miller, L.A., Stephen, N.R., Walker, A.M., Soldatov, A. V., Ireland, T.R., Geraki, K., and Mosselmans, J.F.W. (2017) The limitations of hibonite as a single-mineral oxybarometer for early solar system processes. Chemical Geology, 466, 32–40.

Blander, M., and Fuchs, L.H. (1975) Calcium-aluminum-rich inclusions in the Allende meteorite: evidence for a liquid origin. Geochimica et Cosmochimica Acta, 39, 1605–1619.

Blöchl, P.E., Jepsen, O., and Andersen, O.K. (1994) Improved tetrahedron method for Brillouin-zone integrations. Physical Review B, 49, 16223.

Brearley, A.J., and Jones, R.H. (1998) Chondritic meteorites. Reviews in Mineralogy and Geochemistry, 36, 3–398.

Cameron, A.G.W. (1962) Formation of the solar nebula. Icarus, 1, 339–342.

Connelly, J.N., Bizzarro, M., Krot, A.N., Nordlund, Å., Wielandt, D., and Ivanova, M.A. (2012) The Absolute Chronology and Thermal Processing of Solids in the Solar Protoplanetary Disk. Science, 338, 651–655.

Curien, H., Guillemin, C., Orcel, J.T., and Sternberg, M. (1956) La hibonite, nouvelle espèce minérale. Comptes Rendus Hebdomadaires des Seances de l'Academie des Sciences, 242, 2845–2847.

Doyle, P.M., Schofield, P.F., Berry, A.J., Walker, A.M., and Knight, K.S. (2014) Substitution of Ti3+ and Ti4+ in hibonite (CaAl12O19). American Mineralogist, 99, 1369–1382.

Doyle, P.M., Berry, A.J., Schofield, P.F., and Mosselmans, J.F.W. (2016) The effect of site geometry, Ti content and Ti oxidation state on the Ti K-edge XANES spectrum of synthetic hibonite. Geochimica et Cosmochimica Acta, 187, 294–310.

Ebel, D.S. (2006) Condensation of Rocky Material in Astrophysical Environments. In D.S. Lauretta and H.Y. McSween, Eds., Meteorites and the Early Solar System II Vol. 1, pp. 253–277. University of Arizona Press, Tucson.

Eliezer, I., Eliezer, N., Howald, R.A., and Viswanadham, P. (1981) Thermodynamic Properties of Calcium Aluminates. J. Phys. Chem, 85, 2835–2838.

Eliezer, N. (1982) Reply to Hemingway's Comment on "Thermodynamic Properties of Calcium Aluminates." J. Phys. Chem, 86, 2803–2804.

Eriksson, G., and Pelton, A.D. (1993) Critical evaluation and optimization of the thermodynamic properties and phase diagrams of the CaO-Al2O3, Al2O3-SiO2, and CaO-Al2O3-SiO2 systems. Metallurgical Transactions B, 24, 807–816.

Geiger, C.A., Kleppa, O.J., Mysen, B.O., Lattimer, J.M., and Grossman, L. (1988) Enthalpies of formation of CaAl4O7 and CaAl12O19 (hibonite) by high temperature, alkali borate solution calorimetry. Geochimica et Cosmochimica Acta, 52, 1729–1736.

Giannini, M. (2014) The crystal chemistry of hibonite: an indicator for oxygen fugacity during Solar nebula condensation? Ph. D. thesis. University of Bayreuth.

Glushko, V.P. (1979) Thermal Constants of Matter. Volume IX (Be, Mg, Ca, Sr, Ba, Ra). . Inst. of High Temps. Union Inst. of Scientific and Tech. Information. USSR Academy of Science. Moscow.

Grossman, L. (1972) Condensation in the primitive solar nebula. Geochimica et Cosmochimica Acta, 36, 597–619.

Grossman, L. (2010) Vapor-condensed phase processes in the early solar system. Meteoritics and Planetary Science, 45, 7–20.

Grossman, L., Beckett, J.R., Fedkin, A. V., Simon, S.B., and Ciesla, F.J. (2008) Redox conditions in the solar nebula: Observational, experimental, and theoretical constraints. Reviews in Mineralogy and Geochemistry, 68, 93–140.

Guerch, M.A., Jawed, M., Tariq, G., Jawed, A., Mistry, M., and Asaduzzaman, A. (2024) Compositional-Dependent Structural Parameters and Energetics of Hibonite: Quantum-Chemical Investigation. Journal of Physical Chemistry A.

Hallstedl, B. (1990) Assessment of the CaO-Al2O3 System. Journal of the American Ceramic Society, 73, 15–23.

Han, J., Keller, L.P., Liu, M.C., Needham, A.W., Hertwig, A.T., Messenger, S., and Simon, J.I. (2020) A coordinated microstructural and isotopic study of a Wark-Lovering rim on a Vigarano CAI. Geochimica et Cosmochimica Acta, 269, 639–660.

Han, J., Ohnishi, I., Yasuhara, A., and Keller, L.P. (2022) Atomic-scale structure and non-stoichiometry of meteoritic hibonite: A transmission electron microscope study. American Mineralogist, 107, 873–884.

Hemingway, B.S. (1982) Comment on "Thermodynamic Properties of Calcium Aluminates." J. Phys. Chem, 86, 2802–2803.

Henkelman, G., Arnaldsson, A., and Jónsson, H. (2006) A fast and robust algorithm for Bader decomposition of charge density. Computational Materials Science, 36, 354–360.

Holtstam, D., and Hålenius, U. (2020) Nomenclature of the magnetoplumbite group. Mineralogical Magazine, 84, 376–380.

Kornacki, A.S., and Fegley, B. (1984) Origin of spinel-rich chondrules and inclusions in carbonaceous and ordinary chondrites. Journal of Geophysical Research: Solid Earth, 89, B588–B596.

Kreber, E., Gonser, U., Trautwein, A., and Harris, F.E. (1975) Mössbauer measurements of the bipyramidal lattice site in BaFe12O19. Journal of Physics and Chemistry of Solids, 36, 263–265.

Kresse, G., and Furthmüller, J. (1996) Efficient iterative schemes for ab initio total-energy calculations using a plane-wave basis set. Physical Review B - Condensed Matter and Materials Physics, 54, 11169–11186.

Kresse, G., and Hafner, J. (1993) *Ab initio* molecular dynamics for liquid metals. Physical Review B, 47, 558.

Kumar, R. V., and Kay, D.A.R. (1985) The utilization of galvanic cells using Caβ"-Alumina solid electrolytes in a thermodynamic investigation of the CaO- AI2O3 system. Metallurgical Transactions B, 16, 107–112.

Larimer, J.W. (1967) Chemical fractionations in meteorites-I. Condensation of the elements. Geochimica et Cosmochimica Acta, 31, 1215–1238.

Liu, X.L., Gheno, T., Lindahl, B.B., Lindwall, G., Gleeson, B., and Liu, Z.-K. (2015) First-Principles Calculations, Experimental Study, and Thermodynamic Modeling of the Al-Co-Cr System. (D. Salahub, Ed.)PLOS ONE, 10.

Lodders, K. (2003) Abundances and Condensation Temperatures of the Elements. Meteoritics & Planetary Science, 38, 5272.

Lodders, K., and Palme, H. (2009) Solar system elemental abundances. Meteoritics and Planetary Science Supplement, 72, 5154.

Lu, X.G., Selleby, M., and Sundman, B. (2005) Theoretical modeling of molar volume and thermal expansion. Acta Materialia, 53, 2259–2272.

Lu, X.G., Selleby, M., and Sundman, B (2007) Calculations of thermophysical properties of cubic carbides and nitrides using the Debye–Grüneisen model. Acta Materialia, 55, 1215–1226.

Manga, V.R., and Zega, T.J. (2024) Thermodynamics of ultrarefractory condensates: Implications for the high-temperature limit of the inner dust rim of the early solar protoplanetary disk. Geochimica et Cosmochimica Acta, 367, 133–141.

Manga, V.R., Muralidharan, K., and Zega, T.J. (2022) The interplay between twinning and cation inversion in MgAl2O4-spinel: Implications for a nebular thermochronometer. American Mineralogist, 107, 1470–1476.

Monkhorst, H.J., and Pack, J.D. (1976) Special points for Brillouin-zone integrations. Physical Review B, 13, 5188.

Moruzzi, V.L., Janak, J.F., and Schwarz, K. (1988) Calculated thermal properties of metals. Physical Review B, 37, 790.

Nagashima, M., Armbruster, T., and Hainschwang, T. (2010) A temperature-dependent structure study of gem-quality hibonite from Myanmar. Mineralogical Magazine, 74, 871–885.

Nagata, K., Tanabe, J., and Goto, K. (1989) Standard free energies of formation of CaO-Al2O3 intermediate compounds by means of EMF measurement of galvanic cells. Iron and steel, 75, 2023–2030.

Obradors, X., Collomb, A., Pernet, M., Samaras, D., and Joubert, J.C. (1985) X-ray analysis of the structural and dynamic properties of BaFe12O19 hexagonal ferrite at room temperature. Journal of Solid State Chemistry, 56, 171–181.

Okhotnikov, K., Charpentier, T., and Cadars, S. (2016) Supercell program: a combinatorial structure-generation approach for the local-level modeling of atomic substitutions and partial occupancies in crystals. Journal of Cheminformatics, 8, 17.

Padilha, A.C.M., Osorio-Guillén, J.M., Rocha, A.R., and Dalpian, G.M. (2014) Tin O2n-1 Magnéli phases studied using density functional theory. Physical Review B, 90, 035213.

Pankin, I.A., Kravtsova, A.N., Polozhentsev, O.E., and Soldatov, A. V. (2016) Modelling of substitutional defects in the structure of Ti-bearing hibonite. Journal of Structural Chemistry, 57, 1369–1376.

Perdew, J.P., and Zunger, A. (1981) Self-interaction correction to density-functional approximations for many-electron systems. Physical Review B, 23, 5048.

Perdew, J.P., Burke, K., and Ernzerhof, M. (1996) Generalized gradient approximation made simple. Physical Review Letters, 77, 3865–3868.

Sanville, E., Kenny, S.D., Smith, R., and Henkelman, G. (2007) Improved grid-based algorithm for Bader charge allocation. Journal of Computational Chemistry, 28, 899–908.

Simon, S.B., Grossman, L., and Davis, A.M. (1997) Multiple generations of hibonite in spinel-hibonite inclusions from Murchison. Meteoritics and Planetary Science, 32, 259–269.

Simon, S.B., Davis, A.M., and Grossman, L. (1999) Origin of compact type A refractory inclusions from CV3 carbonaceous chondrites. Geochimica et Cosmochimica Acta, 63, 1233–1248.

Simon, S.B., Sutton, S.R., Grossman, L., and Grossman (2009) First Ti-XANES analyses of refractory inclusions from Murchison. Lpsc, 60637, 1–2.

Tang, W., Sanville, E., and Henkelman, G. (2009) A grid-based Bader analysis algorithm without lattice bias. Journal of Physics Condensed Matter, 21, 84204–84211.

Togo, A., and Tanaka, I. (2018) SPGLib: a software library for crystal symmetry search.

Turchi, P.E.A., Abrikosov, I.A., Burton, B., Fries, S.G., Grimvall, G., Kaufman, L., Korzhavyi, P., Rao Manga, V., Ohno, M., Pisch, A., and others (2007) Interface between quantum-mechanical-based approaches, experiments, and CALPHAD methodology. Calphad, 31, 4–27.

Wang, L., Maxisch, T., and Ceder, G. (2006) Oxidation energies of transition metal oxides within the GGA+U framework. Physical Review B - Condensed Matter and Materials Physics, 73, 195107.

Yoneda, S., and Grossman, L. (1995) Condensation of CaO–MgO–Al2O3–SiO2 liquids from cosmic gases. Geochimica et Cosmochimica Acta, 59, 3413–3444.

Yu, M., and Trinkle, D.R. (2011) Accurate and efficient algorithm for Bader charge integration. Journal of Chemical Physics, 134, 64111.

Zanetta, P.-M., Manga, V.R., Chang, Y.-J., Ramprasad, T., Weber, J., Beckett, J.R., and Zega, T.J. (2023) Atomic-scale characterization of the oxidation state of Ti in meteoritic hibonite: Implications for early solar system thermodynamics. American Mineralogist: Journal of Earth and Planetary Materials, 108, 881–902.

Zega, T., Nittler, L.R., Stroud, R.M., Division, T., and Berkeley, L. (2012) Measurement of the oxidation state of Ti in solar and presolar hibonite. Lunar and Planetary Science 43rd, 9, 4–5.

Zega, T.J., Alexander, C.M.O.D., Nittler, L.R., and Stroud, R.M. (2011) A transmission electron microscopy study of presolar hibonite. The Astrophysical Journal, 730, 83.

Zega, T.J., Manga, V.R., Ciesla, F., Muralidharan, K., Watanabe, K., and Inada, H. (2021) Atomic-scale Evidence for Open-system Thermodynamics in the Early Solar Nebula. The Planetary Science Journal, 2, 115.

Zhang, Y., Kitchaev, D.A., Yang, J., Chen, T., Dacek, S.T., Sarmiento-Pérez, R.A., Marques, M.A.L., Peng, H., Ceder, G., Perdew, J.P., and others (2018) Efficient first-principles prediction of solid stability: Towards chemical accuracy. npj Computational Materials, 4, 9.

Zunger, A., Wei, S.-H., Ferreira, L.G., and Bernard, J.E. (1990) Special quasirandom structures. Physical Review Letters, 65, 353.

9. List of figure captions:

Table 1: Nominal hibonite Wyckoff site and atomic positions from VASP optimization of the reference $CaAl_{12}O_{19}$ (64 atoms) compared to the literature. *Ca is simplified to a central 2d position. **Al2 (M2) is assumed to be on a 2b position before relaxation (z=1/4 or 3/4; see text for detail). *** Nagashima et al. (2010) studied the temperature effects on hibonite atomic positions. Here we compare our 0K calculation to their 296K measurements.

Table 2: The modeled hibonite crystal chemistries and their final parameters after relaxation as discussed in the method section. The bulk Ti oxidation state of the structure is indicated. Total energy and enthalpy of formation according to eq. (2) are given. *Reactions proposed in Zanetta et al. (2023) that impact the bulk Ti oxidation state in the structure (see supplementary material (3)). **Normalized to nominal hibonite. *** R for "random", referring to SQS structures with Ti and Mg randomly distributed on both M3 and M4 sites. N for "nearest", with Ti randomly distributed on M4 sites but the Mg is on the closest M3 site. (u.c.) = unit cell – all other structures are 2x2x1 supercells. (f.u.) = formula unit. Error estimation from previous literature ***(Barin 1995)*** give a difference for reference oxides lower than 5-10 kJ/g-atom.

Table 3: Bader charge analysis of the atomic sites. Variation in Bader charges in equivalent positions are <1%. Ti OS: Ti oxidation state. Bader charge of individual cations of a particular type are averaged per Wyckoff site.

Table 4: Standard enthalpy of formation for hibonite (0 K) compared to previous literature at 298 K and 1 bar.

Fig. 1. Polyhedral representation of the nominal hibonite structure. Small red spheres are oxygen atoms. Large red spheres are Ca. All the other spheres represent the equivalent positions of each M site (Nominally Al), one color per Wyckoff site. The 2b ordered configuration and 4e partially occupied configuration of the M2 site are indicated.

Fig. 2: Representation of the average polyhedral distortion for each Wyckoff site (Table S3). The distortion in each site is represented by a color. The total distortion is visible as the sum of the distortion in each Wyckoff site. The M2 site (brown and orange) and the Ca site (green) are the most represented color and therefore the most distorted sites in the structure.

Fig. 3: Mapping of the polyhedral distortion in the hibonite unit cell. a) Polyhedral distortion map with hibonite structure (transparent) projected along the (100) orientation superimposed (see Fig. S1 for comparison). The color bar shows the amount of polyhedral distortion. The map is constructed based on a data grid containing one point per central atom. The data are then interpolated and averaged along the y axis (orthogonal direction to the plane of the figure). The distortion is maximum for the M2 and M4 sites (see black arrows). The projection along the z axis (plot on the right of the heat map, i.e, summed along the x axis) shows that higher distortion (see red fitted curve) occurs in the R-block. b) Sum of the distortion in the individual blocks as a function of the ground state energy E_0.

Fig. 4: Ternary diagrams for the enthalpy of mixing of the targeted SQS chemistries with Mg, Al, and Ti (sum of both M2 and M4 substitution sites) in pfu. A 3D view is provided to highlight the minimum potential. Red circles represent the calculated compositions (some points exhibit superposition). The surface is interpolated from these points. The scale bar at right applies to both plots. SQS containing oxygen vacancies are indicated by red markers. SQS with no point defects are indicated by blue markers. O vacancies have been accounted by subtracting their concentration in p.f.u to the "substituted species", changing the total used for the normalization of the ternary surface, thus artificially shifting the SQS with O vacancies to slightly higher "Al pfu" (by 0.7 or 0.2 depending if their concentration is 1 or 0.5 pfu respectively). O vacancies significantly affect some regions of the surface (higher $\Delta H_{mixNorm}$).

10. Tables

Table 1

	Wyckoff site		DFT (This work, 0K)	Doyle et al., 2014 (0K)	Nagashima et al., 2010 (296K)***	*Diff.* *Doyle et al. 2014*	*Diff.* *Nagashima 2010*
Ca	***2d****	*x*	0.6667	0.6667	0.6667	*0.0000*	*0.0000*
		y	0.3333	0.3333	0.3333	*0.0000*	*0.0000*
		z	0.2500	0.2500	0.2500	*0.0000*	*0.0000*
Al1 (M1)	***2a***	*x*	0.0000	0.0000	0.0000	*0.0000*	*0.0000*
		y	0.0000	0.0000	0.0000	*0.0000*	*0.0000*
		z	0.0000	0.0000	0.0000	*0.0000*	*0.0000*
Al2 (M2)	***2b****	*x*	0.0000	0.0000	0.0000	*0.0000*	*0.0000*
		y	0.0000	0.0000	0.0000	*0.0000*	*0.0000*
		z	0.2500	0.2500	0.2572	*0.0000*	*0.0072*
Al3 (M3)	***4f***	*x*	0.3333	0.3333	0.3333	*0.0000*	*0.0000*
		y	0.6667	0.6667	0.6667	*0.0000*	*0.0000*
		z	0.0283	0.0273	0.0276	*-0.0010*	*-0.0007*
Al4 (M4)	***4f***	*x*	0.3333	0.3333	0.3333	*0.0000*	*0.0000*
		y	0.6667	0.6667	0.6667	*0.0000*	*0.0000*
		z	0.1913	0.1902	0.1892	*-0.0011*	*-0.0021*
Al5 (M5)	***12k***	*x*	0.1682	0.1687	0.1679	*0.0005*	*-0.0003*
		y	0.8318	0.8313	0.8321	*-0.0005*	*0.0003*
		z	0.8903	0.8912	0.8920	*0.0009*	*0.0017*
O1	***4e***	*x*	0.0000	0.0000	0.0000	*0.0000*	*0.0000*
		y	0.0000	0.0000	0.0000	*0.0000*	*0.0000*
		z	0.1509	0.1511	0.1505	*0.0002*	*-0.0004*
O2	***4f***	*x*	0.3333	0.3333	0.3333	*0.0000*	*0.0000*
		y	0.6667	0.6667	0.6667	*0.0000*	*0.0000*
		z	0.9455	0.9454	0.9427	*-0.0001*	*-0.0028*
O3	***6h***	*x*	0.1816	0.1839	0.1803	*0.0023*	*-0.0013*
		y	0.8184	0.8161	0.8197	*-0.0023*	*0.0013*
		z	0.2500	0.2500	0.2500	*0.0000*	*0.0000*
O4	***12k***	*x*	0.1551	0.1565	0.1523	*0.0014*	*-0.0028*
		y	0.8449	0.8435	0.8477	*-0.0014*	*0.0028*
		z	0.0525	0.0524	0.0531	*-0.0001*	*0.0007*
O5	***12k***	*x*	0.5034	0.5035	0.5040	*0.0001*	*0.0006*
		y	0.4966	0.4965	0.4960	*-0.0001*	*-0.0006*
		z	0.1498	0.1499	0.1499	*0.0001*	*0.0001*

Table 2

	SQS n°		Final lattice parameter a/b (Å)	Final lattice parameter c (Å)	Final lattice parameter Volume (Å^3)	Ti OS	E_0 (eV/u.c.)	**Δhmix (KJ/mol) from Elements**	Δhmix (kJ/mol) from oxides	**Diff. to nominal hib. from oxides**
	0	Nominal $CaAl_{12}O_{19}$ (u.c.)	5.61	22.10	695.64	Ø	-237.92	**-10644.24**	-57.23	**0.00**
No point defects (reactions 1, 2, 5)*	1	$CaAl_{10}Ti_{(M2)1}Mg_{(M3)1}Ti_{(M4)0}O_{19}$	11.31	22.27	2849.93	4+	-239.60	**-10630.14**	-125.21	**-67.98**
	2	$CaAl_{10}Ti_{(M2)0}Mg_{(M3)1}Ti_{(M4)1}O_{19}$ **R****	11.34	22.33	2871.95	4+	-239.51	**-10621.95**	-117.03	**-59.79**
	3	$CaAl_{10}Ti_{(M2)0}Mg_{(M3)1}Ti_{(M4)1}O_{19}$ **N****	11.34	22.32	2867.90	4+	-239.52	**-10622.86**	-117.93	**-60.70**
	4	$CaAl_{10}Ti_{(M2)0.5}Mg_{(M3)1}Ti_{(M4)0.5}O_{19}$ **R****	11.22	22.09	2778.79	4+	-239.42	**-10613.28**	-108.35	**-51.12**
	5	$CaAl_{10}Ti_{(M2)0.5}Mg_{(M3)1}Ti_{(M4)0.5}O_{19}$ **N****	11.21	22.08	2776.49	4+	-239.41	**-10612.23**	-107.31	**-50.08**
	6	$CaAl_{10}Ti_{(M2)1}Mg_{(M3)0}Ti_{(M4)1}O_{19}$	11.28	22.21	2824.60	3+	-243.68	**-10423.80**	80.80	**138.03**
	7	$CaAl_{7.5}Ti_{(M2)1}Mg_{(M3)2}Ti_{(M4)1.5}O_{19}$	11.32	22.29	2854.99	1:4	-240.57	**-10548.41**	-125.56	**-68.33**
	8	$CaAl_{11}Ti_{(M2)0}Mg_{(M3)0}Ti_{(M4)1}O_{19}$	11.32	22.30	2859.47	3+	-240.89	**-10542.36**	3.44	**60.68**
	9	$CaAl_{8}Ti_{(M2)1}Mg_{(M3)2}Ti_{(M4)1}O_{19}$	11.43	22.51	2940.31	4+	-240.58	**-10549.09**	-126.25	**-69.02**
	10	$CaAl_{8}Ti_{(M2)0}Mg_{(M3)2}Ti_{(M4)2}O_{19}$	11.46	22.41	2943.60	4+	-240.82	**-10576.78**	-153.94	**-96.70**
	11	$CaAl_{7}Ti_{(M2)1}Mg_{(M3)2}Ti_{(M4)2}O_{19}$	11.5	22.64	2994.05	1:2	-243.95	**-10486.18**	-104.54	**-47.30**
Oxygen vacancies (Reactions 3, 4, 6)*	12	$CaAl_{11}Ti_{(M2)0}Mg_{(M3)1}Ti_{(M4)0}O_{18.5}$	11.19	22.03	2757.55	Ø	-230.05	**-10301.82**	52.52	**109.75**
	13	$CaAl_{10}Ti_{(M2)0}Mg_{(M3)2}Ti_{(M4)0}O_{18}$	11.24	22.13	2794.39	Ø	-222.25	**-9966.89**	154.78	**212.01**
	14	$CaAl_{10}Ti_{(M2)0}Mg_{(M3)1}Ti_{(M4)1}O_{18.5}$	11.22	22.10	2784.56	3+	-233.65	**-10261.23**	51.90	**109.13**
	15	$CaAl_{10}Ti_{(M2)1}Mg_{(M3)1}Ti_{(M4)0}O_{18.5}$	11.20	22.06	2767.90	3+	-233.65	**-10261.78**	51.36	**108.59**
	16	$CaAl_{8}Ti_{(M2)0}Mg_{(M3)2}Ti_{(M4)2}O_{18.5}$	11.34	22.33	2872.18	1:1	-235.06	**-10221.52**	9.54	**66.77**

Table 3

SQS n°	**SQS formula**	**Ti OS**	Ca	Al	$Mg_{(M3)}$	$Ti_{(M2)}$	$Ti_{(M4)}$	O1	O2	O3	O4	O5
0	Nominal $CaAl_{12}O_{19}$		1.64	3.00				-1.99	-2.00	-1.93	-2.02	-1.96
6	$CaAl_{10}Ti_{(M2)1}Mg_{(M3)0}Ti_{(M4)1}O_{19}$	3+	1.63	3.00		2.22	2.30	-1.94	-1.99	-1.60	-2.02	-1.89
8	$CaAl_{11}Ti_{(M2)0}Mg_{(M3)0}Ti_{(M4)1}O_{19}$	3+	1.65	3.00			2.26	-2.00	-1.99	-1.82	-2.02	-1.89
9	$CaAl_{8}Ti_{(M2)1}Mg_{(M3)2}Ti_{(M4)1}O_{19}$	4+	1.65	3.00	2.00	2.57	2.66	-1.74	-1.83	-1.65	-1.96	-1.84
10	$CaAl_{8}Ti_{(M2)0}Mg_{(M3)2}Ti_{(M4)2}O_{19}$	4+	1.67	3.00	2.00		2.67	-1.97	-1.98	-1.65	-2.00	-1.69
16	$CaAl_{8}Ti_{(M2)0}Mg_{(M3)2}Ti_{(M4)2}O_{18.5}$	1:1	1.66	3.00	2.00		2.59	-2.01	-2.00	-1.68	-2.06	-1.74

Table 4

Reference	ΔHf0 (298 K ; from elements) kJ.mol-1	
Glushko (1979)	-10742.8	± 12.9
Eliezer et al. (1982)	-10605.2	± 10
Hemingway (1982)	-10813.0	± 20
Geiger (1988)	-10722.0	± 12
Hallstedl (1990)	-10711.5	
Erikson & Pelton (1993)	-10704.2	
This study (0K)	-10644.2	

11. Figures

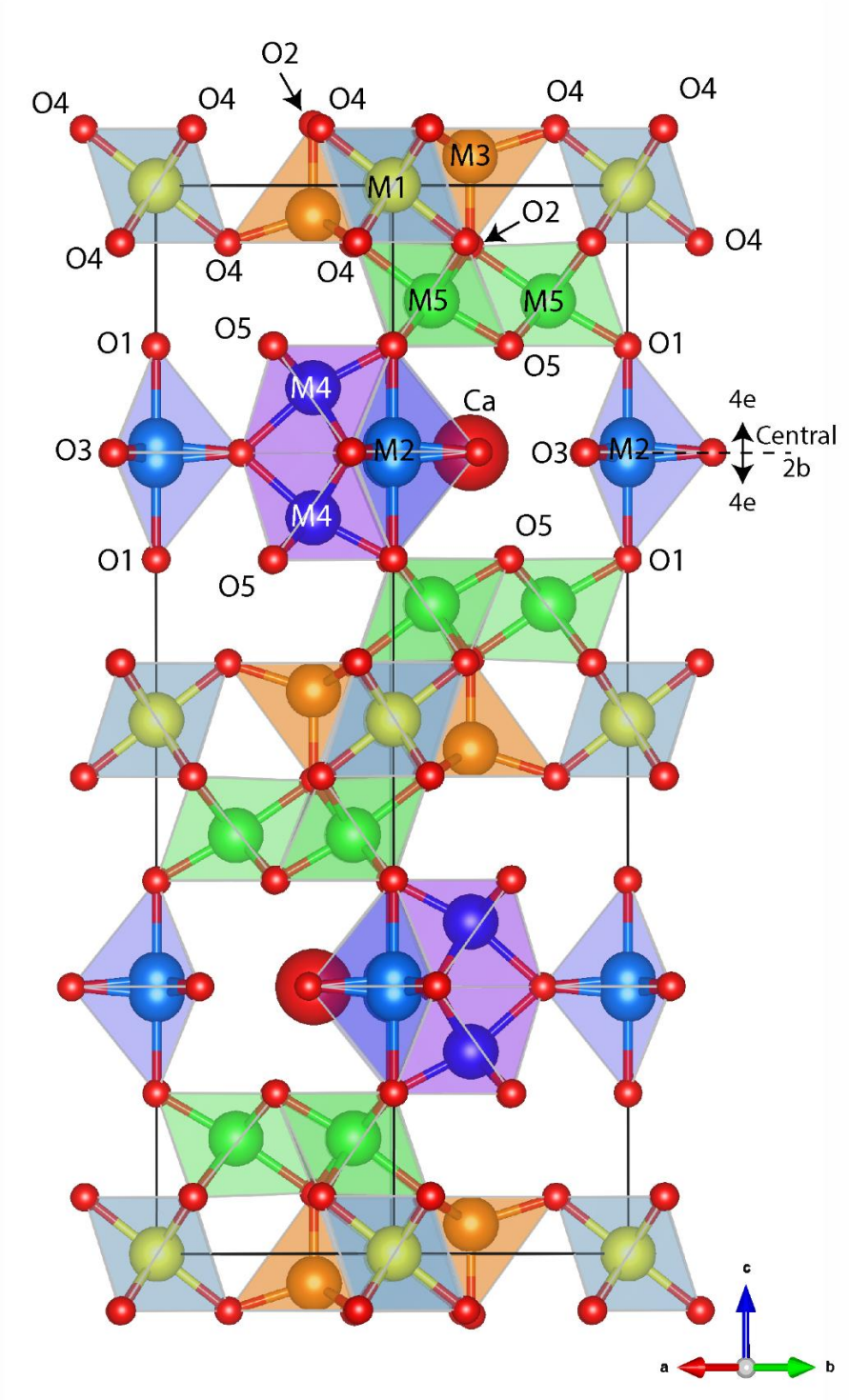

Fig. 1

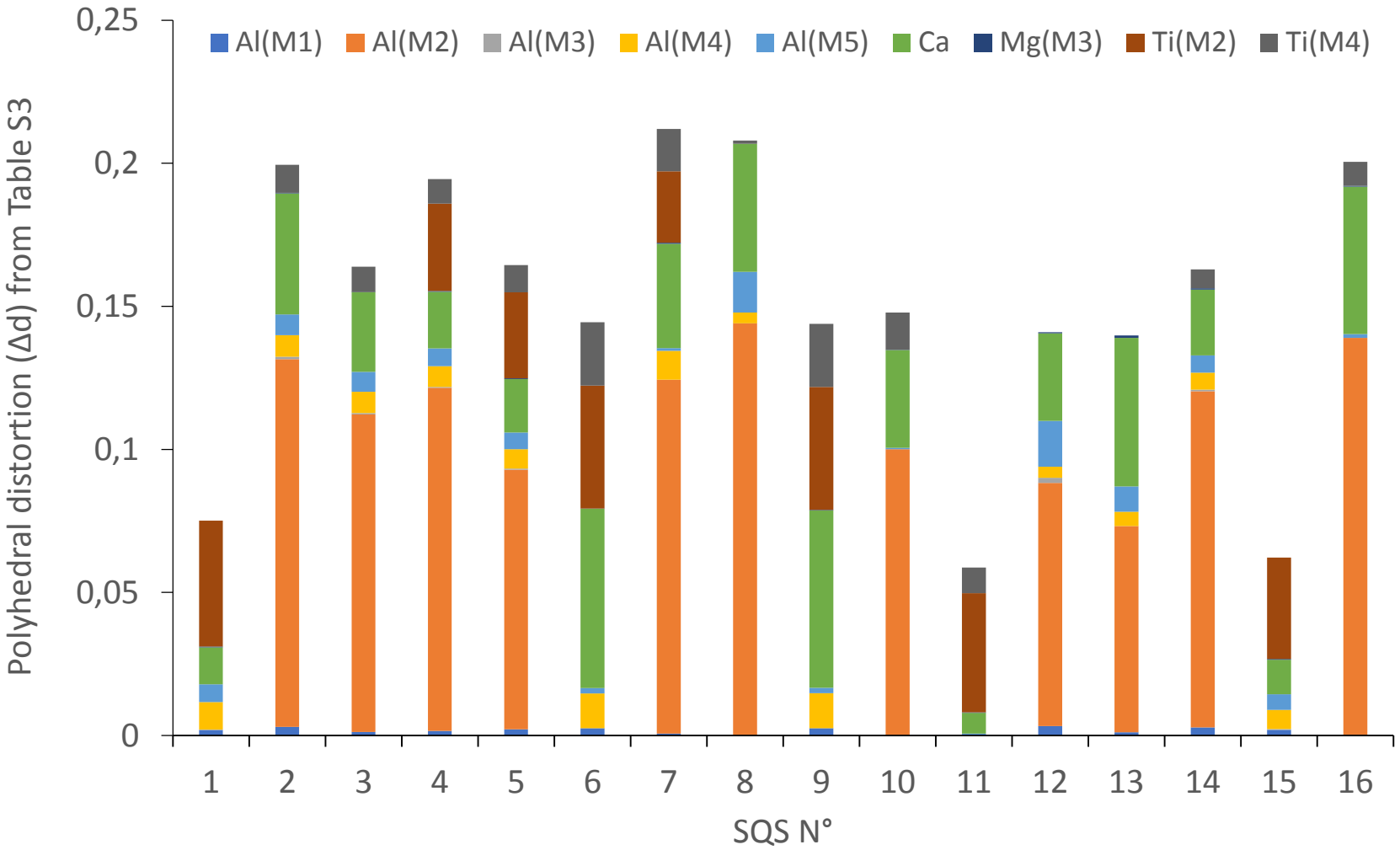
Al(M1)
Al(M2)
Al(M3)
Al(M4)
Al(M5)
Ca
Mg(M3)
Ti(M2)
Ti(M4)
Polyhedral distortion (Δd) from Table S3
0,25
0,2
0,15
0,1
0,05
0
1
2
3
4
5
6
7
8
9
10
11
12
13
14
15
16
SQS N°

Fig. 2

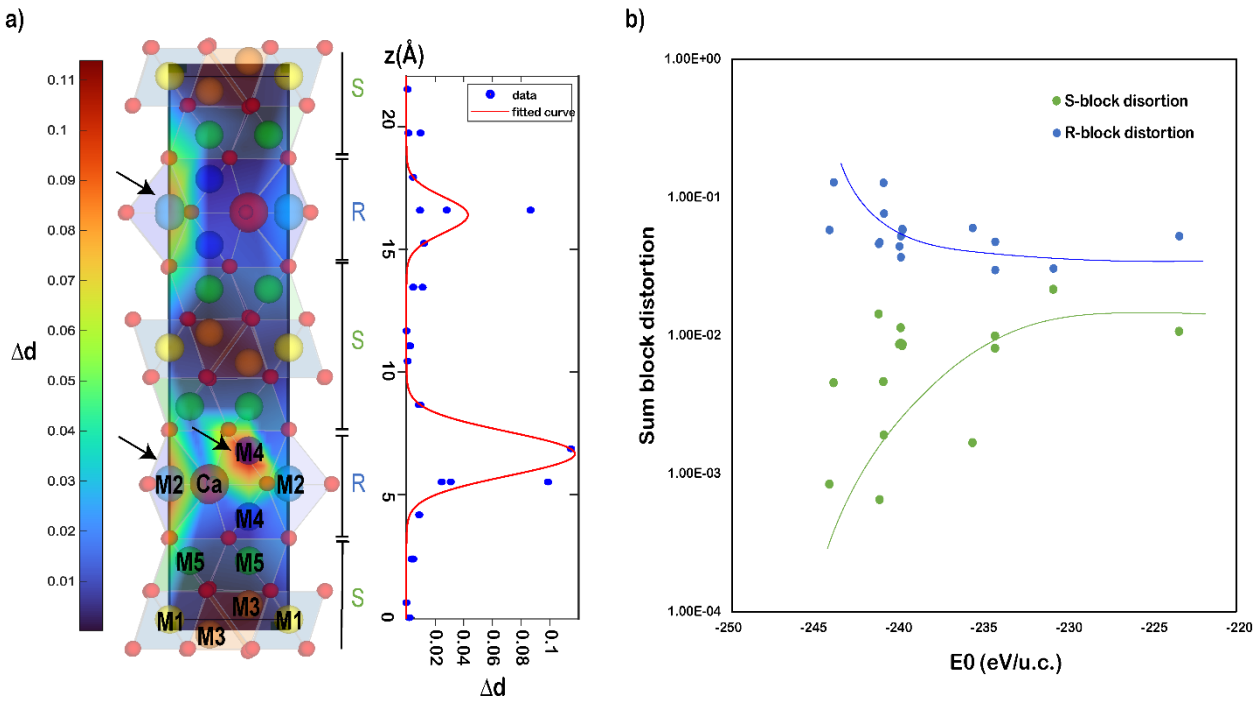
a)
b)
Δd
z(Å)
data
fitted curve
S
R
S
R
S
M4
M2
Ca
M2
M4
M5
M5
M1
M3
M1
M3
Δd
Sum block distortion
S-block disortion
R-block distortion
E0 (eV/u.c.)

Fig. 3

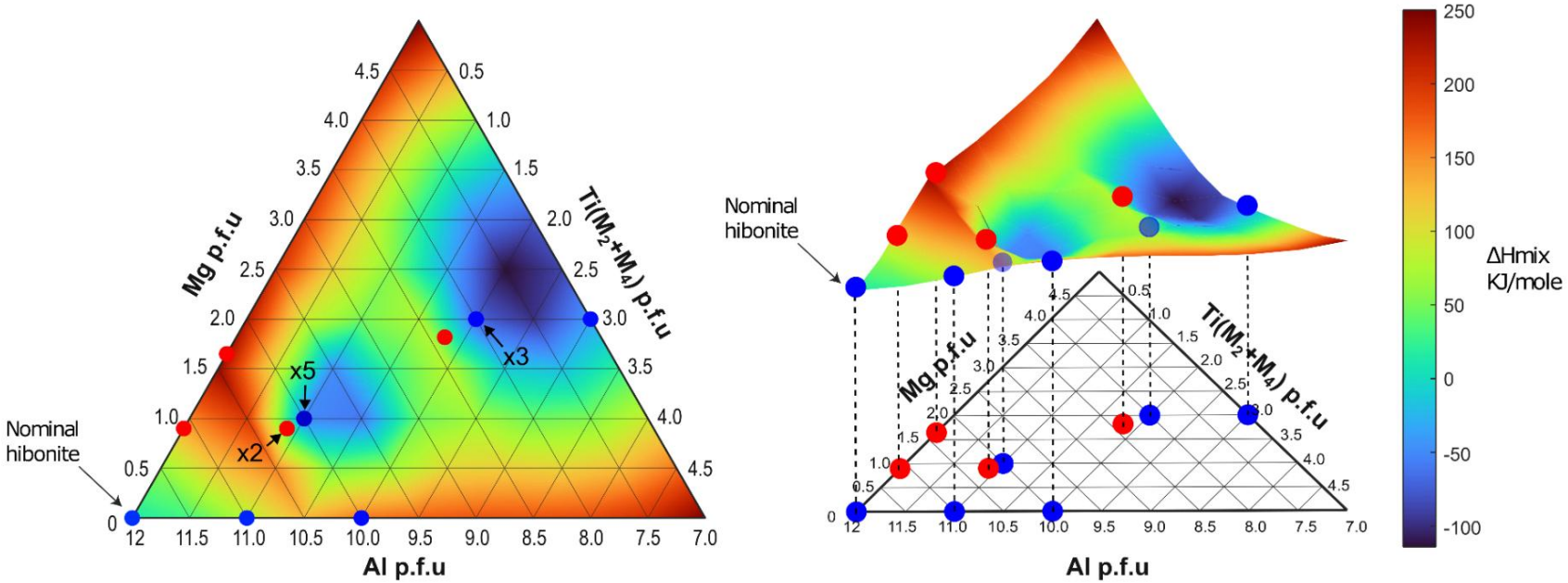
Nominal hibonite
x5
x2
x3
Mg p.f.u
Ti(M2+M4) p.f.u
Al p.f.u
ΔHmix KJ/mole

Fig. 4